Triple-Mode Wide-Input Range Resonant DC–DC Converter With Extended Asymmetric Modulation

Sangoh Kim, *Student Member, IEEE*, Junseong Cho, *Student Member, IEEE*, Jong-Woo Kim, *Member, IEEE*, Minsung Kim, *Senior Member, IEEE*, and Byeongcheol Han, *Member, IEEE*

***Abstract*—This article proposes a triple-mode resonant converter operating over a wide input voltage range for renewable energy harvesting applications. The proposed converter operates in a pure series-resonant mode with a nominal input voltage, an asymmetric resonant boost mode with a low-input voltage, and an asymmetric pulse-width-modulation series-resonant buck mode with a high-input voltage. This converter adopts an asymmetric half-bridge-type voltage-doubler to reduce the transformer turns ratio and number of active components. Moreover, its extended asymmetric modulation reduces hard switching turn-ON losses compared to conventional symmetric modulations. Consequently, the proposed converter attains high power conversion efficiency and power density over a wide input voltage range. The operating principles and steady-state analysis are presented in detail herein. Finally, a 300-W/380-V prototype is presented to validate the feasibility of the proposed converter over an input voltage range of 30–60 V.**

***Index Terms*—Asymmetric modulation, buck–boost converter, isolated resonant converter, renewable energy, soft switching.**

I. Introduction

As increased attention is dedicated to the mitigation of issues such as environmental pollution and energy depletion, the demand for renewable energy sources also increases. Generally, because renewable energy modules such as photovoltaic and thermoelectric energy sources generate a relatively low dc voltage (30–60 V), a step-up dc–dc converter is often required to converter the low dc voltage to a high dc-bus voltage (380 V) that can be used for battery packs, uninterruptible power supplies, or utility grids [1]. Moreover, because the output voltage of renewable energy sources has fluctuating characteristics, the step-up dc–dc converter must operate over a wide input voltage range with high efficiency [2], [3]. Furthermore, a high-frequency switching operation in an isolated converter can aid in the realization of a more compact power system [4]. Several isolated step-up converters have been proposed to meet the abovementioned requirements. Such isolated step-up converters can be classified into step-up pulse-width-modulation (PWM) converters and step-up resonant converters.

Among conventional PWM converters, a flyback dc–dc converter is considered as an ideal candidate owing to an isolation, a simple structure, low cost, and achieving a high voltage gain with a relatively low duty cycle [5]. But, the leakage inductance of its transformer induces a high-voltage spike and a high switching loss at the main switch. To resolve these issues, flyback-derived converters using quasi-square-wave control [6], [7], active clamp circuits, and auxiliary cells [8], [9], [10], [11] have been proposed. In [6] and [7], they achieved zero-voltage switching (ZVS) to reduce switching losses, but the leakage energy could not be recycled, resulting in additional losses and voltage spikes. An active clamp circuit or an auxiliary cell [8], [9], [10], [11] can improve the efficiency by completely recycling the leakage inductance along with soft switching. However, such converters still suffer from high turn-OFF losses, and their complexities and costs increase owing to the use of auxiliary switch devices and resonant tanks.

Alternatively, resonant converters serve as good candidates for soft switching to achieve high efficiency. A dual-series-resonant converter [12], wherein its active clamp circuit is combined with a flyback converter, has been proposed. The converter excites the transformer bidirectionally for improved utilization of the transformer, and it can also operate as a boost converter with a reduced turns ratio of the transformer. However, to achieve a sufficiently high voltage gain, an extremely large duty cycle is required, which makes secondary diodes suffer from severe reverse recovery problems. Furthermore, a considerable voltage imbalance among the resonant capacitors causes a high voltage stress on the resonant capacitors. This imbalance makes it more difficult to design a resonance circuit because it puts switching devices and resonant capacitors under high voltage stress. A high step-up resonant converter with an active voltage doubler has been suggested to realize a voltage balance among the resonant capacitors at a fixed duty ratio of 0.5 [13].

Manuscript received 29 August 2022; revised 6 January 2023; accepted 5 February 2023. Date of publication 16 February 2023; date of current version 20 April 2023. This work was supported in part by the National Research Foundation of Korea (NRF) funded by the Korea Government (MSIT) under Grant 2022R1F1A1065488 and in part by the Korea Electric Power Corporation under Grant R22XO02-26. Recommended for publication by Associate Editor J. M. Alonso.*(Corresponding author: Byeongcheol Han.)*

Sangoh Kim is with the School of Electronic and Electrical Engineering, Kyungpook National University, Daegu 41566, South Korea (e-mail: aks4539@knu.ac.kr).

Junseong Cho is with the System Development Center, Hanwha Solution, Daegu 41756, South Korea (e-mail: Junseong.Cho@qcells.com).

Jong-Woo Kim is with the Department of Electrical and Electronics Engineering, Konkuk University, Seoul 05029, South Korea (e-mail: jongwookim@konkuk.ac.kr).

Minsung Kim is with the Division of Electronics and Electrical Engineering, Dongguk University, Seoul 04620, South Korea (e-mail: mkim@dgu.ac.kr).

Byeongcheol Han is with the School of Electronics Engineering and the School of Electronic and Electrical Engineering, Kyungpook National University, Daegu 41566, South Korea (e-mail: hbychol@knu.ac.kr).

Color versions of one or more figures in this article are available at https://doi.org/10.1109/TPEL.2023.3245622.

Digital Object Identifier 10.1109/TPEL.2023.3245622

To reduce the hard switching turn-ON losses, a utilization of bidirectional ac switches in an active voltage doubler structure has been proposed [14], [15]; moreover, an asymmetric modulation method has also been proposed to decrease the number of hard switching turn-ON times [16].

However, the abovementioned resonant converters explicitly operate as only a boost converter; hence, they cannot be applied when the input voltage is higher than nominal voltage. Therefore, hybrid-mode resonant converters [17], [18], [19], [20], [21] have been proposed to attain the desired output voltage over a wide input voltage range. Such converters are capable of operating not only in the boost mode but also in the buck mode. In cases where the input voltage is lower than a nominal value, the converter operates as a PWM resonant converter by fixing the primary-side switch's duty cycle to 0.5 and controlling the secondary-side switch's duty cycle; otherwise, it works as a phase-shifted full-bridge resonant converter through the variable duty cycle of the primary switch. The hybrid-mode full bridge converters using an ac bidirectional switch are proposed to operate in wide input voltage range [17], [18]. However, such converters require two additional switches, and their switch utilization is poor because these switches are operated only in the boost mode. The idea of using an active voltage doubler in a hybrid-mode resonant converter was proposed for attaining a high power conversion efficiency [19]. The active voltage doubler structure reduces the number of active components and implements a high-step-up operation. However, the number of devices is still large owing to the use of a full-bridge circuit on the primary side. In addition, the hard switching turn-ON of the secondary side switches occurs twice in the boost mode, thereby resulting in considerable switching losses. Recently, a bridgeless hybrid converter [20], [21] has been proposed to achieve high efficiency. It can achieve not only ZVS at the primary and secondary side switches but also zero-current switching (ZCS) of the secondary diodes to reduce the switching loss across all modes of operation. However, the limited range of the ZVS region, high reverse recovery of the secondary diode, and high-voltage ringing make it challenging to attain high power conversion efficiency and a high power density. Besides, the turns ratio of the transformer is doubled compared with that of the aforementioned voltage doubler structures.

Herein, this article proposes a triple-mode resonant converter with extended asymmetric modulation for application in renewable energy harvesting. The proposed triple-mode resonant converter functions in different modes by comparing the input voltage with a nominal value in order to operate over a wide input voltage range, which are as follows:

1) asymmetric resonant boost (ARB) mode under a low-input voltage;
2) pure series-resonant (PSR) mode under a nominal-input voltage;
3) asymmetric PWM series-resonant buck (APSRB) mode under a high-input voltage.

The proposed converter employs a flyback topology with an active clamp circuit at the low-voltage side and an asymmetric half-bridge type voltage-doubler at the high-voltage side; thus, the converter comprises only three switches and one diode with a low transformer turns ratio to minimize the size and cost of the converter circuit. In addition, with the aid of extended asymmetric modulation, the converter can significantly reduce hard-switching turn-ON losses of the rectifier while keeping the small number of switch components. Therefore, the proposed converter can retain the desired output voltage over a wide input voltage range with low component counts and high efficiency. This article presents detailed converter operation, steady-state characteristics, and design process. During our study, we built a converter prototype operating over an input voltage range of 30–60 V, at a dc-bus voltage of 380 V, at a rated power of 300 W, and demonstrated its performance.

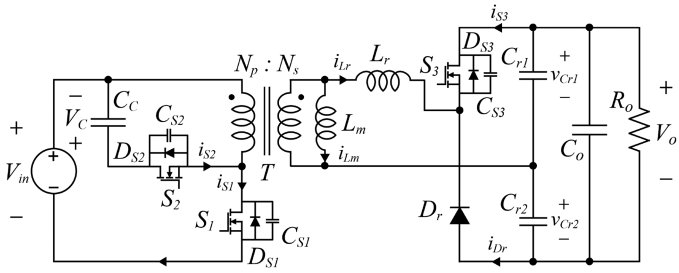

Fig. 1. Circuit diagram of the proposed triple-mode resonant DC–DC converter.

The rest of this article is organized as follows. The topology and triple-mode operations of the proposed converter are introduced in Section II, and a steady-state analysis is presented in Section III. The design process for the proposed converter is provided in Section IV. Experimental results are presented in Sections V, and VI summarizes this article.

II. Converter Operation

A. Topology Description

The propose proposed triple-mode resonant dc–dc converter has switches S_1 and S_2 with a clamp capacitor C_c on the primary side of the transformer T. The secondary side of T has a half-bridge circuit with an asymmetric structure by employing resonant capacitors C_{r1} and C_{r2}, a switch S_3, and a resonant diode D_r, and a resonant inductor L_r that comprises the leakage inductance of the transformer T and a supplementary inductor (see Fig. 1). To simplify the circuit operation, the following assumptions were made.

1) Switches S_1, S_2, and S_3 are ideal with the exception of their reverse body diodes D_{S1}, D_{S2}, and D_{S3}, and output capacitances C_{S1} and C_{S2}.
2) Capacitors C_c and C_o are large enough so that their capacitor voltages V_C and V_o exhibit no voltage ripple.
3) Transformer T is ideal except for magnetizing inductance L_m and leakage inductance.
4) Resonant capacitors C_{r1} and C_{r2} are identical; $C_{r1} = C_{r2}$

For simple analysis, we define the output capacitance $C_{\rm oss} = C_{S1} = C_{S2}$ of a switch component and $C_r = C_{r1} + C_{r2}$. The operating modes of the proposed resonant converter can be categorized into ARB, PSR, and APSRB modes by comparing the input voltage $V_{\rm in}$ with nominal voltage $V_{\rm nom}$.

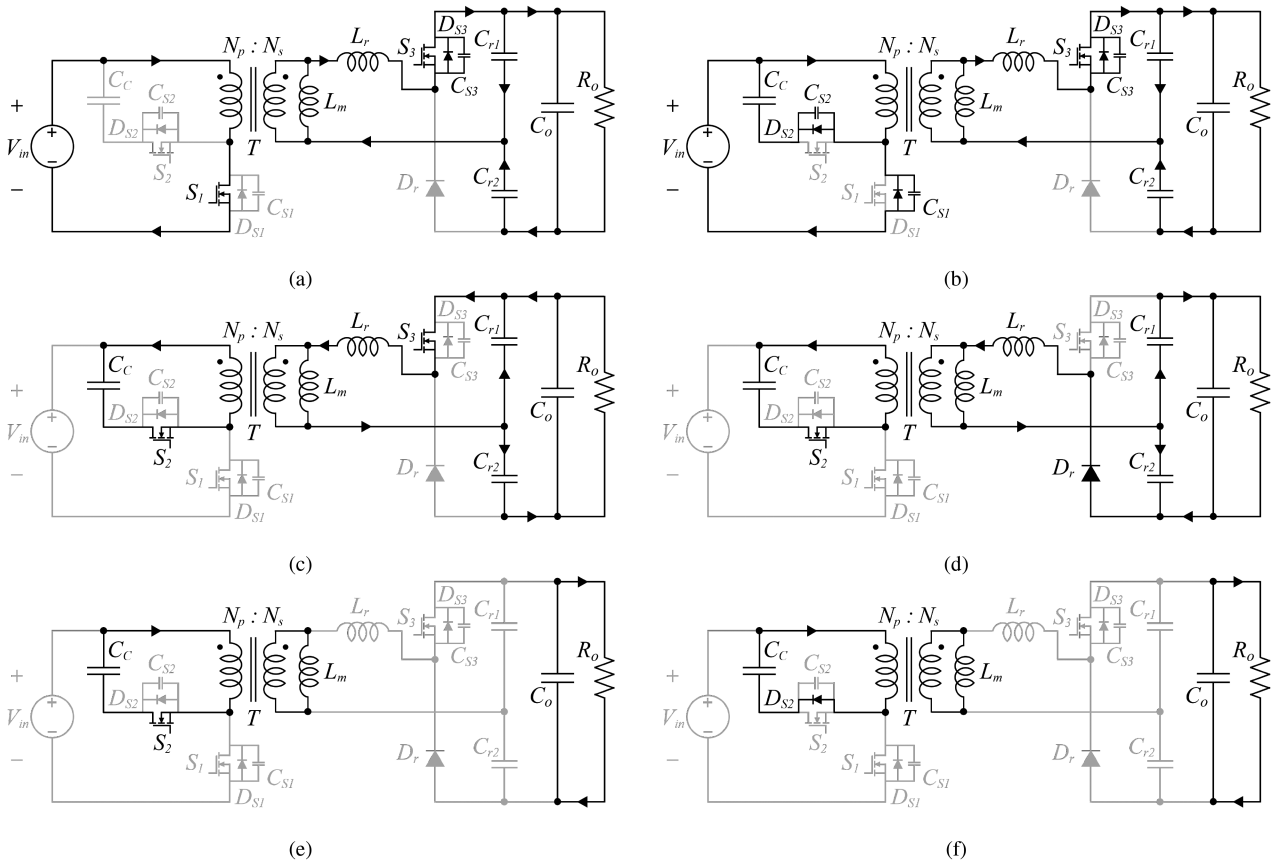

Fig. 2. Operating stages in the ARB mode. (a)–(f) Stages 1–6.

B. ARB Mode ($V_{\rm in} < V_{\rm nom}$)

1) *Stage 1 [t_0, t_1]*: At time t_0 [see Fig. 2(a)], S_1 and S_3 are turned ON, and $V_{\rm in}$ is applied to the primary-side winding of T. i_{Lr} starts to flow, and v_{Cr} starts to increase from its minimum value. i_{Lr} resonates based on the resonance between L_r and C_r. In Stage 1, $V_{\rm in}$, L_r, C_{r1}, and C_{r2} constitute the LC equivalent resonance circuit, and its equation can be derived as

$$L_r \frac{di_{Lr}(t)}{dt} = nV_{\rm in} - v_{Cr1}(t) \tag{1}$$

$$i_{Lr}(t) = C_{r1}\frac{dv_{Cr1}(t)}{dt} - C_{r2}\frac{dv_{Cr2}(t)}{dt} \tag{2}$$

where $i_{Lr}(t_0) = 0$ and $v_{Cr}(t_0) = < v_{Cr} > - \Delta v_{Cr}$ where $< v_{Cr} >$ denotes the average value of v_{Cr}, and Δv_{Cr} is the voltage ripple of v_{Cr}. Because V_o is constant, $i_{Lr}(t)$ can be obtained as follows:

$$i_{Lr}(t) = C_{r1}\frac{dv_{Cr1}(t)}{dt} - C_{r2}\frac{d(V_o - v_{Cr1}(t))}{dt}$$

$$= C_r \frac{dv_{Cr1}(t)}{dt}. \tag{3}$$

Solving (1) and (3) yields the following:

$$i_{Lr}(t) = \frac{r_1}{Z_r}\sin\left[\omega_r(t-t_0)\right] \tag{4}$$

$$v_{Cr1}(t) = nV_{\rm in} - r_1\cos\left[\omega_r(t-t_0)\right] \tag{5}$$

where $r_1 = nV_{\rm in} - < v_{Cr} > + \Delta v_{Cr}$ denotes the radius of the circular path with the center at $(nV_{\rm in}, 0)$ [see Fig. 4(a)]. During stage 1, the operating point on the state-plane trajectory moves from A_1 to A_2, and the resonant frequency and characteristic impedance can be expressed as

$$\omega_r = \frac{1}{\sqrt{L_r(C_{r1}+C_{r2})}} = \frac{1}{\sqrt{L_r C_r}} \tag{6}$$

$$Z_r = \sqrt{\frac{L_r}{C_{r1}+C_{r2}}} = \sqrt{\frac{L_r}{C_r}}. \tag{7}$$

Stage 1 ends at half of the switching cycle, and stage 2 begins with zero current. The duration of stage 1 is represented as $D_{\rm pri}T_s$ where $D_{\rm pri}$ and T_s represent primary-side switch S_1's duty ratio and switching period, respectively.

2) *Stage 2 [t_1, t_2]*: At time t_1 [see Fig. 2(b)], S_1 is turned OFF and the converter enters the deadtime area. After a given deadtime, S_2 is turned ON using ZVS. During stage 2, the operating point on the state-plane trajectory remains at A_2 [see Fig. 4(a)].

3) *Stage 3 [t_2, t_3]*: At time t_2 [see Fig. 2(c)], S_2 is turned ON with achieving ZVS because D_{S2} conducts in stage 2. i_{Lr} starts to flow, and v_{Cr} starts to drop from its maximum

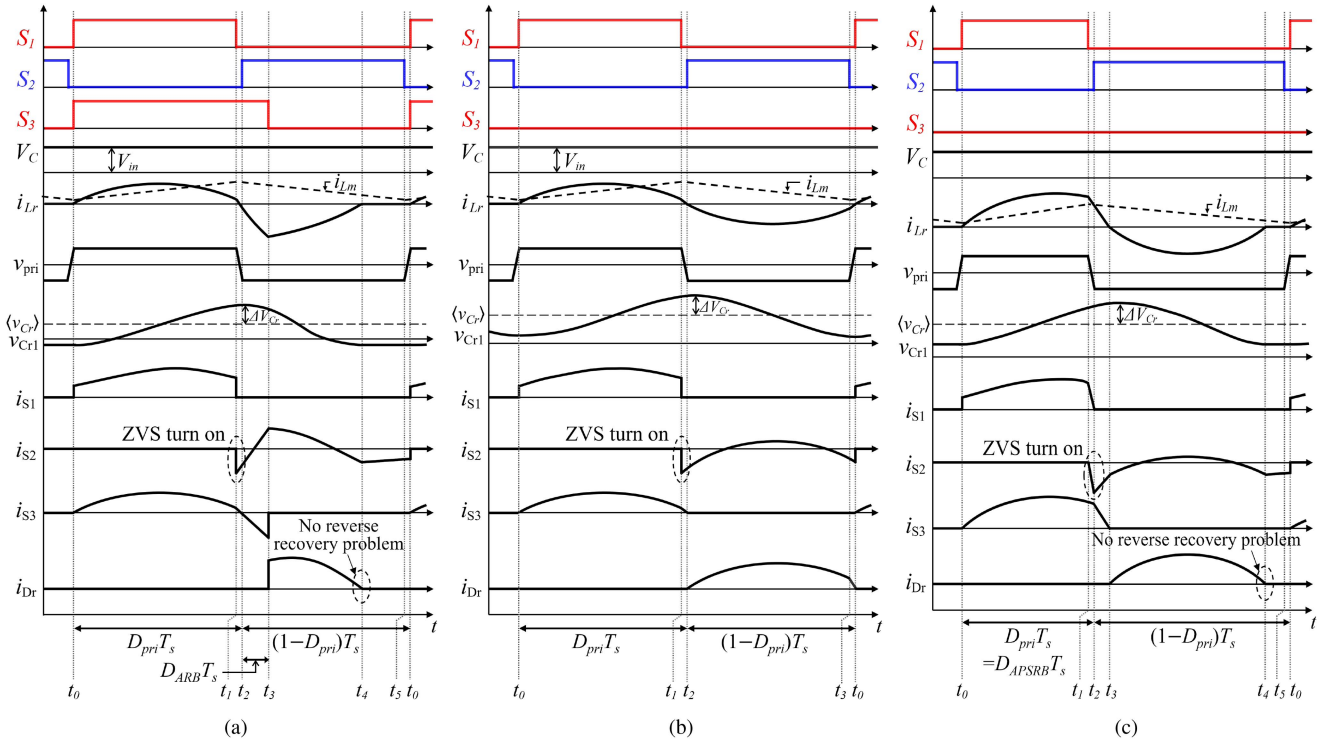

Fig. 3. Theoretical waveforms of the proposed converter operating in the (a) ARB mode, (b) PSR mode, and (c) APSRB mode.

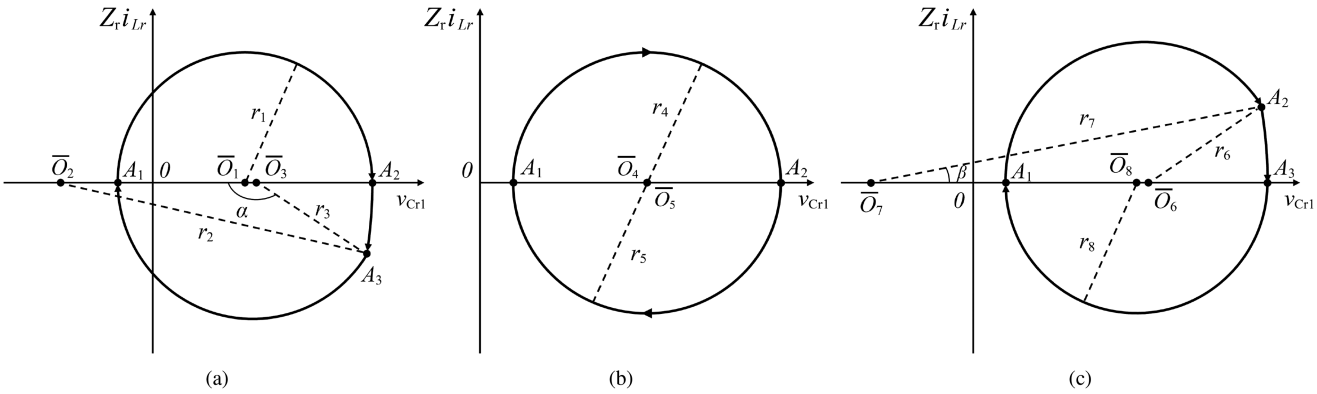

Fig. 4. State-plane trajectory diagrams of the equivalent resonance circuit operating in the (a) ARB mode, (b) PSR mode, and (c) APSRB mode.

value. During stage 3, C_C, L_r, C_{r1}, and C_{r2} constitute the LC equivalent resonance circuit, and its equation can be written as

$$L_r \frac{di_{Lr}(t)}{dt} = -nV_C - v_{Cr1}(t) \tag{8}$$

$$i_{Lr}(t) = C_r \frac{dv_{Cr1}(t)}{dt} \tag{9}$$

where $i_{Lr}(t_2) = 0$ and $v_{Cr}(t_2) =< v_{Cr} > +\Delta v_{Cr}$. Because the period in stage 2 is extremely short, it can be ignored, and $i_{Lr}(t_2)$ can be considered to be zero. Solving (8) and (9) yields the following:

$$i_{Lr}(t) = \frac{r_2}{Z_r} \sin\left[\omega_r(t - t_2)\right] \tag{10}$$

$$v_{Cr1}(t) = -nV_C + r_2 \cos\left[\omega_r(t - t_2)\right] \tag{11}$$

where $r_2 = nV_C + < v_{Cr} > +\Delta v_{Cr}$ denotes the radius of the circular path with the center at $(-nV_C, 0)$ [see Fig. 4(a)]. During stage 3, the operating point on the state-plane trajectory moves from A_2 to A_3 [see Fig. 4(a)]. The duration of stage 3 is represented as $D_{\mathrm{ARB}}T_s$ where D_{ARB} represents boosting duty ratio [see Fig. 3(a)].

4) *Stage 4 [t_3, t_4]*: At time t_3 [see Fig. 2(d)], S_2 is still turned ON; additionally, the rectifier diode D_r is also turned ON after S_3 is turned OFF. i_{Lr} increased in the previous stage is transferred to the output load. During this stage, V_C, V_o, C_{r1}, C_{r2}, and L_r constitute an LC equivalent resonance circuit, and i_{Lr} approaches zero, following the sinusoidal

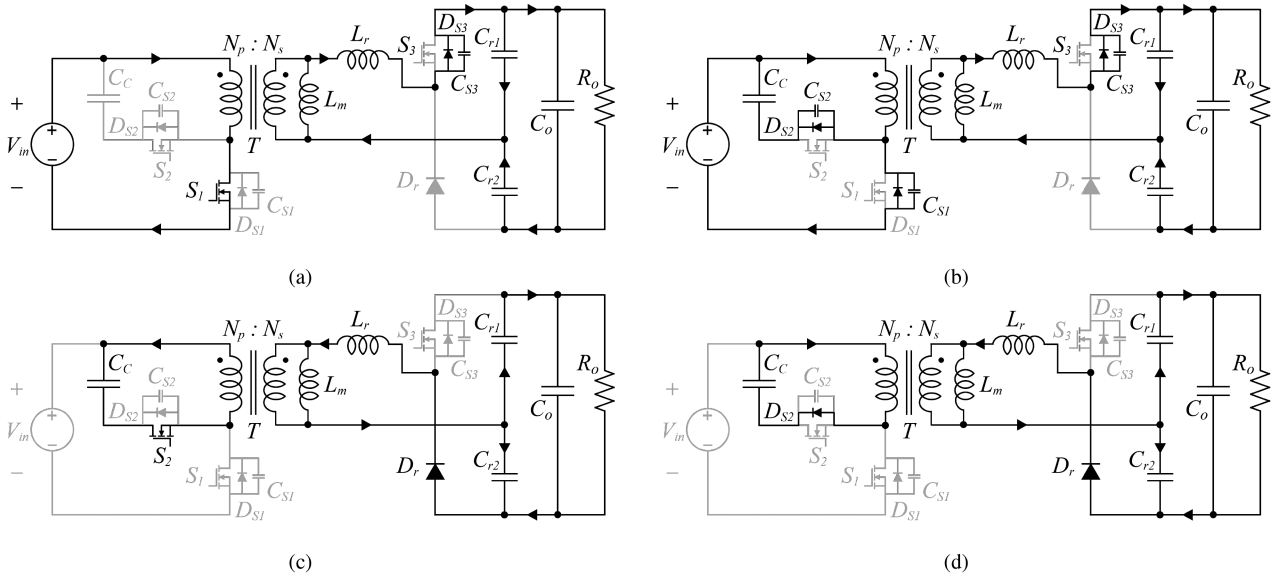

Fig. 5. Operating stages in the PSR mode. (a)–(d) Stages 1–4.

waveform. The equation of the equivalent circuit can be derived as

$$L_r \frac{di_{Lr}(t)}{dt} = -nV_C + V_o - v_{Cr1}(t) \tag{12}$$

$$i_{Lr}(t) = C_r \frac{dv_{Cr1}(t)}{dt} \tag{13}$$

where $i_{Lr}(t_3) = -\frac{r_3}{Z_r}\sin\alpha$ and $v_{Cr}(t_3) = -nV_C + V_o - r_3\cos\alpha$ where $\alpha = \sin^{-1}(\frac{r_2}{r_3}\sin[\omega_r(t_3 - t_2)])$. Solving (12) and (13) yields the following:

$$i_{Lr}(t) = -\frac{r_3}{Z_r}\sin\left[\alpha - \omega_r(t - t_3)\right] \tag{14}$$

$$v_{Cr1}(t) = -nV_C + V_o - r_3\cos\left[\alpha - \omega_r(t - t_3)\right] \tag{15}$$

where $r_3 = -nV_C + V_o - < v_{Cr} > + \Delta v_{Cr}$ denotes the radius of the circular path with the center at $(-nV_C + V_o, 0)$ [see Fig. 4(a)]. And, during stage 4, the operating point on the state-plane trajectory moves from A_3 to A_1.

5) *Stage 5 [t_4, t_5]*: At time t_4 [see Fig. 2(e)], D_r is turned OFF with ZCS. i_{Lr} becomes zero, and v_{Cr} stays at its minimum value. During stage 5, the primary-side reflection of i_{Lm} is equivalent to the current flowing through S_2. The operating point on the state-plane trajectory remains at A_1 [see Fig. 4(a)].
6) *Stage 6 [t_5, t_0]*: At time t_5 [see Fig. 2(f)], S_2 is turned OFF and the converter enters a deadtime area. The state-plane trajectory still remains at point A_1 during stage 6 [see Fig. 4(a)].

C. PSR Mode ($V_{\rm in} = V_{\rm nom}$)

1) *Stage 1 [t_0, t_1]* : At time t_0 [see Fig. 5(a)], i_{Lr} starts to flow, and v_{Cr} starts to increase from its minimum value, similar to that in stage 1 in the ARB mode. During this stage, $V_{\rm in}$, L_r, C_{r1}, and C_{r2} constitute the LC equivalent resonance circuit, and its equation can be derived as

$$L_r \frac{di_{Lr}(t)}{dt} = nV_{\rm in} - v_{Cr1}(t) \tag{16}$$

$$i_{Lr}(t) = C_r \frac{dv_{Cr1}(t)}{dt} \tag{17}$$

where $i_{Lr}(t_0) = 0$, and $v_{Cr}(t_0) = < v_{Cr} > - \Delta v_{Cr}$. Solving (16) and (17) yields the following:

$$i_{Lr}(t) = \frac{r_4}{Z_r}\sin\left[\omega_r(t - t_0)\right] \tag{18}$$

$$v_{Cr1}(t) = nV_{\rm in} - r_4\cos\left[\omega_r(t - t_0)\right] \tag{19}$$

where $r_4 = nV_{\rm in} - < v_{Cr} > + \Delta v_{Cr}$ denotes the radius of the circular path with the center at $(nV_{\rm in}, 0)$ [see Fig. 4(b)]. Because $< v_{Cr} >$ is the same as $\frac{V_o}{2}$ in the PSR mode, we can consider that $r_4 = \Delta v_{Cr}$. During stage 1, the operating point on the state-plane trajectory shifts from A_1 to A_2 [see Fig. 4(b)]. The duration of stage 1 is represented as $D_{\rm pri}T_s$ where $D_{\rm pri}$ represents primary-side switch S_1's duty ratio [see Fig. 3(b)].
2) *Stage 2 [t_1, t_2]*: At time t_1 [see Fig. 5(b)], S_1 is turned OFF and the converter enters a deadtime area. After a given deadtime, S_2 is turned ON using ZVS. During stage 2, the operating point on the state-plane trajectory remains at A_2 [see Fig. 4(b)].
3) *Stage 3 [t_2, t_3]*: At time t_2 [see Fig. 5(c)], S_2 is turned ON with achieving ZVS because D_{S2} conducts in stage 2. i_{Lr} starts to flow, and v_{Cr} starts to drop from its maximum value. In stage 3, C_C, V_o, L_r, C_{r1}, and C_{r2} constitute the LC equivalent resonance circuit, and its equation can be written as

$$L_r \frac{di_{Lr}(t)}{dt} = -nV_C + V_o - v_{Cr1}(t) \tag{20}$$

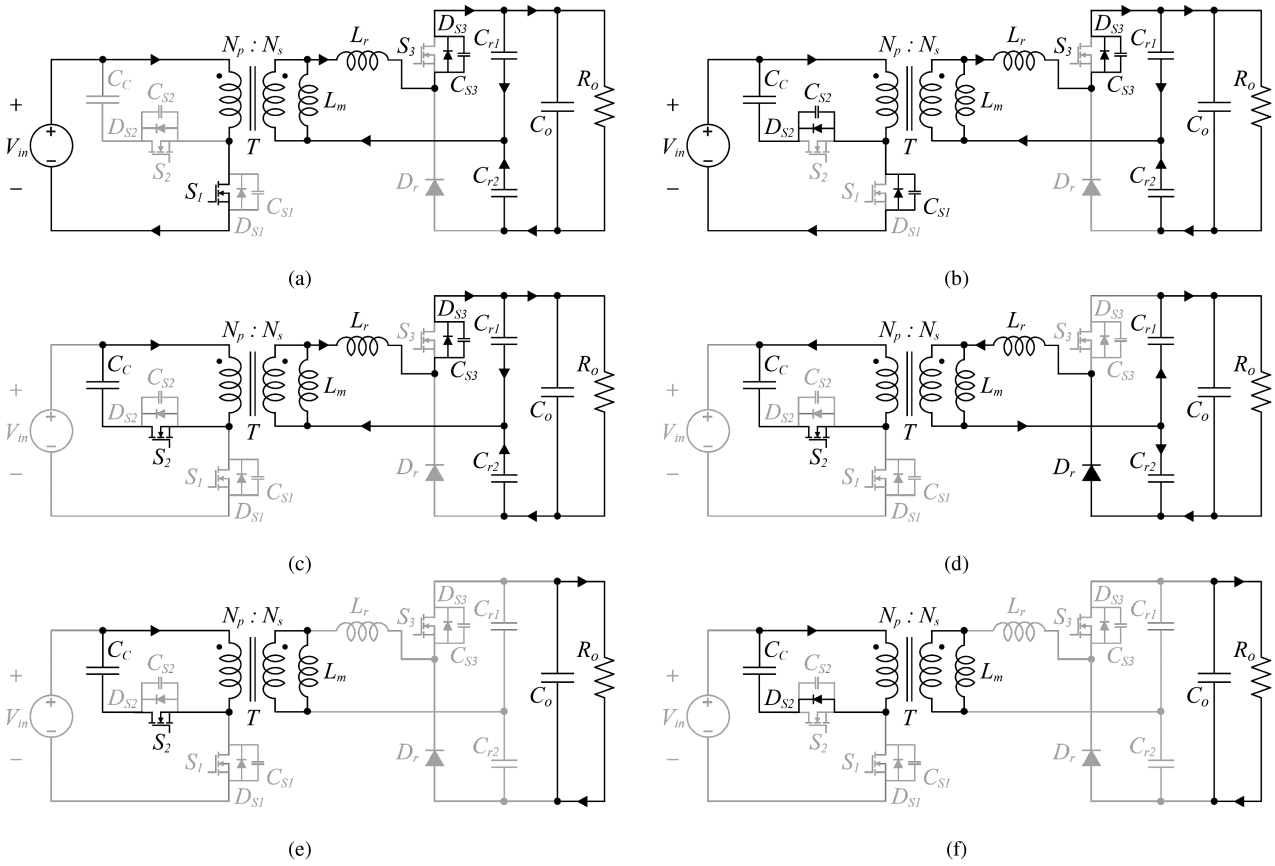

Fig. 6. Operating stages in the APSRB mode. (a)–(f) Stages 1–6.

$$i_{Lr}(t) = C_r \frac{dv_{Cr1}(t)}{dt} \tag{21}$$

where $i_{Lr}(t_2) = 0$ and $v_{Cr}(t_2) = < v_{Cr} > + \Delta v_{Cr}$. Solving (20) and (21) yields the following:

$$i_{Lr}(t) = -\frac{r_5}{Z_r} \sin\left[\omega_r(t - t_2)\right] \tag{22}$$

$$v_{Cr1}(t) = -nV_C - r_5 \cos\left[\omega_r(t - t_2)\right] \tag{23}$$

where $r_5 = nV_C - V_o + < v_{Cr} > + \Delta v_{Cr}$ denotes the radius of the circular path with the center at $(-nV_C + V_o, 0)$ [see Fig. 4(b)]. Because $< v_{Cr} >$ is the same as $\frac{V_o}{2}$ in the PSR mode, we can consider that $r_5 = \Delta v_{Cr}$. The operating point on the state-plane trajectory shifts from A_2 to A_1 [see Fig. 4(b)].

4) *Stage 4 [t_3, t_4]*: At time t_3 [see Fig. 5(d)], D_r is turned OFF with ZCS. i_{Lr} becomes zero and v_{Cr} is at its minimum value. The operating point on the state-plane trajectory remains at A_1 [see Fig. 4(b)].

D. APSRB Mode ($V_{\text{in}} > V_{\text{nom}}$)

1) *Stage 1 [t_0, t_1]* : At time t_0 [see Fig. 6(a)], i_{Lr} starts to flow, and v_{Cr} starts to increase from its minimum value, similar to that in stage 1 in the PSR mode. In stage 1, V_{in}, L_r, C_{r1}, and C_{r2} constitute the LC equivalent resonance circuit and its equation can be written as

$$L_r \frac{di_{Lr}(t)}{dt} = nV_{\text{in}} - v_{Cr1}(t) \tag{24}$$

$$i_{Lr}(t) = C_r \frac{dv_{Cr1}(t)}{dt} \tag{25}$$

where $i_{Lr}(t_0) = 0$, and $v_{Cr}(t_0) = < v_{Cr} > - \Delta v_{Cr}$. Solving (24) and (25) yields the following:

$$i_{Lr}(t) = \frac{r_6}{Z_r} \sin\left[\omega_r(t - t_0)\right] \tag{26}$$

$$v_{Cr1}(t) = nV_{\text{in}} - r_6 \cos\left[\omega_r(t - t_0)\right] \tag{27}$$

where $r_6 = nV_{\text{in}} - < v_{Cr} > + \Delta v_{Cr}$ denotes the radius of the circular path with the center at $(nV_{\text{in}}, 0)$ [see Fig. 4(c)]. During stage 1, the operating point on the state-plane trajectory moves from A_1 to A_2 [see Fig. 4(c)]. The duration of stage 1 is represented as $D_{\text{APSRB}}T_s$ where D_{APSRB} represents duty ratio of the APSRB mode, which is the same as primary-side switch S_1's duty ratio D_{pri} [see Fig. 3(c)].

2) *Stage 2 [t_1, t_2]*: At time t_1 [see Fig. 6(b)], S_1 is turned OFF, and the converter enters a deadtime area. After a given deadtime, S_2 is turned ON using ZVS. During stage 2, the operating point on the state-plane trajectory remains at A_2 [see Fig. 4(c)].

3) *Stage 3 [t_2, t_3]*: At time t_2 [see Fig. 6(c)], S_2 is turned ON with achieving ZVS because D_{S2} conducts in stage 2. However, the direction of i_{Lr} is the same as that in stage 2. C_C, L_r, C_{r1}, and C_{r2} constitute the LC equivalent resonance circuit and its equation can be written as

$$L_r \frac{di_{Lr}(t)}{dt} = -nV_C - v_{Cr1}(t) \tag{28}$$

$$i_{Lr}(t) = C_r \frac{dv_{Cr1}(t)}{dt} \tag{29}$$

where $i_{Lr}(t_2) = \frac{r_7}{Z_r}\sin\beta$, $v_{Cr}(t_2) = -nV_C + r_7\cos\beta$, and $\beta = \sin^{-1}(\frac{r_6}{r_7}\sin[\omega_r(t_2 - t_0)])$. Solving (28) and (29) yields the following:

$$i_{Lr}(t) = \frac{r_7}{Z_r}\sin\left[\beta - \omega_r(t - t_2)\right] \tag{30}$$

$$v_{Cr1}(t) = -nV_C + r_7\cos\left[\beta - \omega_r(t - t_2)\right] \tag{31}$$

where $r_7 = nV_C + < v_{Cr} > + \Delta v_{Cr}$ denotes the radius of the circular path with the center at $(-nV_C, 0)$ [see Fig. 4(c)]. During stage 3, the operating point on the state-plane trajectory shifts from A_2 to A_3 [see Fig. 4(c)].

4) *Stage 4 [t_3, t_4]*: At time t_3 [see Fig. 6(d)], S_2 is still turned ON and D_r is also turned ON, similar to that in stage 4 in the ARB mode. i_{Lr} starts to flow, and v_{Cr} starts to drop from its maximum value. In stage 4, C_C, V_o, L_r, C_{r1}, and C_{r2} constitute the LC equivalent resonance circuit, and its equation can be written as

$$L_r \frac{di_{Lr}(t)}{dt} = -nV_C + V_o - v_{Cr1}(t) \tag{32}$$

$$i_{Lr}(t) = C_r \frac{dv_{Cr1}(t)}{dt} \tag{33}$$

where $i_{Lr}(t_3) = 0$ and $v_{Cr}(t_3) = < v_{Cr} > + \Delta v_{Cr}$. Solving (32) and (33) yields the following:

$$i_{Lr}(t) = -\frac{r_8}{Z_r}\sin\left[\omega_r(t - t_3)\right] \tag{34}$$

$$v_{Cr1}(t) = -nV_C + V_o + r_8\cos\left[\omega_r(t - t_3)\right] \tag{35}$$

where $r_8 = nV_C - V_o + < v_{Cr} > + \Delta v_{Cr}$ denotes the radius of the circular path with the center at $(-nV_C + V_o, 0)$ [see Fig. 4(c)]. During stage 4, the operating point on the state-plane trajectory shifts from A_3 to A_1 [see Fig. 4(c)].

5) *Stage 5 [t_4, t_5]*: At time t_4 [see Fig. 6(e)], D_r is turned OFF with ZCS. i_{Lr} becomes zero, and v_{Cr} stays at its minimum value. During stage 5, the primary-side reflection of i_{Lm} is equivalent to the current flowing through S_2. The operating point on the state-plane trajectory remains at A_1 [see Fig. 4(c)].

6) *Stage 6 [t_5, t_0]*: At time t_5, S_2 is turned OFF, and the converter enters a deadtime area [see Fig. 6(f)]. The state-plane trajectory remains at point A_1 during this stage.

III. Steady-State Analysis

A. Voltage Gain of ARB Mode

For calculation of the voltage gain of the ARB mode, we first figure out the value of Δv_{Cr}. As the same amount of power is transferred during two half-cycles, only arcs A_1 to A_2 are considered [see Fig. 4(a)]. The average value of i_{Lr} is twice the average value of the output current. Subsequently

$$\begin{aligned} I_o = \frac{V_o}{R_o} &= \frac{1}{T_s}\left[\int_{t_0}^{t_1}\frac{r_1}{Z_r}\sin\left[\omega_r(\tau - t_0)\right]d\tau\right] \\ &= \frac{1}{T_s Z_r \omega_r}\left(-r_1\cos\left[\omega_r(t_1 - t_0)\right] + r_1\right) \\ &= \frac{2\Delta v_{Cr}}{T_s Z_r \omega_r} = \frac{2C_r\Delta v_{Cr}}{T_s}. \end{aligned} \tag{36}$$

Since the radius of the semicircle in stage 1 of the ARB mode equals the voltage ripple of v_{Cr} [see Fig. 4(a)], it can be written as $r_1 = \Delta v_{Cr}$. Rearranging (36) for Δv_{Cr} yields the following:

$$\Delta v_{Cr} = r_1 = \frac{P_o T_s}{2V_o C_r} \tag{37}$$

where $P_o = V_o I_o$. From the state-plane trajectory diagram [see Fig. 4(a)], $v_{Cr}(t_0)$ and $v_{Cr}(t_2)$ can be described as

$$v_{Cr}(t_0) = \overline{O}_1 - r_1 = nV_{\text{in}} - \frac{P_o T_s}{2V_o C_r} \tag{38}$$

$$v_{Cr}(t_2) = \overline{O}_1 + r_1 = nV_{\text{in}} + \frac{P_o T_s}{2V_o C_r}. \tag{39}$$

r_2 can also be described by calculating the distance between $\overline{O}_2$ and $v_{Cr}(t_2)$ as follows:

$$r_2 = v_{Cr}(t_2) + \left|\overline{O}_2\right| = 2nV_{\text{in}} + \frac{P_o T_s}{2V_o C_r}. \tag{40}$$

From (11), $v_{Cr}(t_3)$ can be described by using the boosting duty ratio D_{ARB} as follows:

$$\begin{aligned} v_{Cr}(t_3) &= \overline{O}_2 + r_2\cos(w_r D_{\text{ARB}} T_s) \\ &= -nV_C + r_2\cos(w_r D_{\text{ARB}} T_s). \end{aligned} \tag{41}$$

r_3 can be expressed as

$$\begin{aligned} r_3 &= \overline{O}_3 - v_{Cr}(t_0) = \overline{O}_3 - [\overline{O}_1 - r_1] \\ &= V_o - 2V_{\text{in}} + \frac{P_o T_s}{2nV_{\text{in}} C_r}. \end{aligned} \tag{42}$$

As the two circles intersect at point A_3 at time t_3 [see Fig. 4(a)], applying the cosine law to the triangle $\overline{O}_2\overline{O}_3 A_3$ yields the following:

$$r_3^2 = r_2^2 + (\overline{O}_3 - \overline{O}_2)^2 - 2r_2(\overline{O}_3 - \overline{O}_2)\cos(w_r D_{\text{ARB}} T_s). \tag{43}$$

The required boosting duty ratio is

$$\begin{aligned} D_{\text{ARB}} &= \frac{1}{w_r T_s}\cos^{-1}\left[\frac{r_2^2 - r_3^2 + V_o^2}{2r_2 V_o}\right] \\ &= \frac{1}{w_r T_s}\cos^{-1}\left[\frac{2C_r V_o^2 + (2 - M_{\text{ARB}})P_o T_s}{2C_r V_o^2 + P_o T_s M_{\text{ARB}}}\right] \end{aligned} \tag{44}$$

where $M_{\mathrm{ARB}} = V_o/(2nV_{\mathrm{in}})$ denotes the voltage gain in the ARB mode. Rearranging (44) for M_{ARB} yields the following:

$$M_{\mathrm{ARB}} = \frac{2A + 2B}{2B - AB} \tag{45}$$

where $A = 1 - \cos(\frac{2\pi D_{\mathrm{ARB}}}{F})$; $B = \frac{2\pi Q}{F}$; and $F = \frac{f_s}{f_r}$ with f_r and f_s representing the resonant frequency and the switching frequency, respectively; the quality factor is

$$Q = \frac{w_r L_r}{R_o} = \frac{1}{w_r C_r R_o}. \tag{46}$$

B. Voltage Gain of APSRB Mode

Similar to the voltage gain calculation approach employed for the ARB mode, we consider only the second-half switching cycle. Then

$$\begin{aligned} I_o = \frac{V_o}{R_o} &= \frac{1}{T_s}\left[\int_{t_3}^{t_4}\left|-\frac{r_8}{Z_r}\sin\left[w_r(\tau - t_3)\right]\right| d\tau\right] \\ &= \frac{1}{T_s Z_r \omega_r}\left|r_8\cos\left[\omega_r(t_4 - t_3)\right] - r_8\right| \\ &= \frac{2\Delta v_{Cr}}{T_s Z_r w_r} = \frac{2C_r\Delta v_{Cr}}{T_s}. \end{aligned} \tag{47}$$

Since the radius of this semicircle in stage 4 of the APSRB mode equals the voltage ripple of v_{Cr}, it can be written as $r_8 = \Delta v_{Cr}$ [see Fig. 4(c)]. Rearranging (47) for Δv_{Cr} yields the following:

$$\Delta v_{Cr} = r_8 = \frac{P_o T_s}{2V_o C_r} \tag{48}$$

where $P_o = V_o I_o$. From the state-plane trajectory diagram [see Fig. 4(c)], $v_{Cr}(t_0)$ and $v_{Cr}(t_3)$ can be described as

$$v_{Cr}(t_0) = \overline{O}_8 - r_8 = -nV_C + V_o - \frac{P_o T_s}{2V_o C_r} \tag{49}$$

$$v_{Cr}(t_3) = \overline{O}_8 + r_8 = -nV_C + V_o + \frac{P_o T_s}{2V_o C_r}. \tag{50}$$

r_7 can also be described by calculating the distance between $\overline{O}_7$ and $v_{Cr}(t_3)$ as follows:

$$r_7 = v_{Cr}(t_3) + \left|\overline{O}_7\right| = V_o + \frac{P_o T_s}{2V_o C_r}. \tag{51}$$

$v_{Cr}(t_2)$ can be described by the buck duty ratio D_{APSRB} as follows:

$$\begin{aligned} v_{Cr}(t_2) &= \overline{O}_6 - r_6\cos(w_r D_{\mathrm{APSRB}} T_s) \\ &= nV_{\mathrm{in}} - r_6\cos(w_r D_{\mathrm{APSRB}} T_s). \end{aligned} \tag{52}$$

r_6 can be expressed as

$$\begin{aligned} r_6 &= \overline{O}_6 - v_{Cr}(t_0) = \overline{O}_6 - [\overline{O}_8 - r_8] \\ &= nV_{\mathrm{in}} + nV_C - V_o + \frac{P_o T_s}{2V_o C_r}. \end{aligned} \tag{53}$$

As the two circles intersect at point A_2 at time $t_1 = t_2$ [see Fig. 4(c)], applying the cosine law to the triangle $\overline{O}_6\overline{O}_7 A_2$ yields the following:

$$r_7^2 = r_6^2 + (\overline{O}_6 - \overline{O}_7)^2 - 2r_6(\overline{O}_6 - \overline{O}_7)\cos(w_r D_{\mathrm{APSRB}} T_s). \tag{54}$$

The required buck duty ratio is

$$D_{\mathrm{APSRB}} = \frac{1}{w_r T_s}\cos^{-1}\left[\frac{r_6^2 - r_7^2 + (nV_{\mathrm{in}} + nV_C)^2}{2r_6(nV_{\mathrm{in}} + nV_C)}\right]. \tag{55}$$

Rearranging (55) for the voltage gain in the APSRB mode [i.e., $M_{\mathrm{APSRB}} = V_o/(2nV_{\mathrm{in}})$] yields the following:

$$M_{\mathrm{APSRB}} = \frac{(B-2)A' + \sqrt{\{(B-2)A'\}^2 + 16A'B}}{8B(1 - D_{\mathrm{APSRB}})} \tag{56}$$

where $A' = 1 - \cos(\frac{2\pi D_{\mathrm{APSRB}}}{F})$.

By using the obtained voltage gain equations in (45) and (56), a 3-D voltage gain graph can be constructed with respect to Q and D (see Fig. 7). Herein, duty cycle D indicates $0.5 + D_{\mathrm{ARB}}$, 0.5, and D_{APSRB} at ARB, PSR, and APSRB mode, respectively. So, the output voltage can be retained constantly over the wide input voltage range by adjusting duty cycle D based on the given quality factor Q.

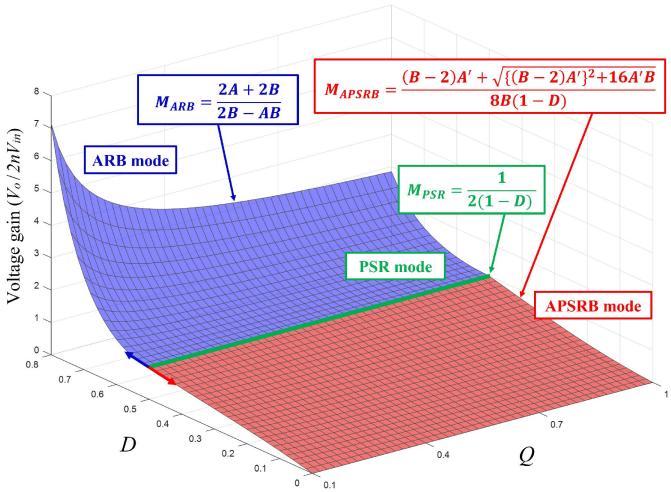

Fig. 7. Voltage gain graph in different modes. Blue, red, and green surfaces represent the voltage gains of ARB, APSRB, and PSR modes, respectively.

IV. Design Guideline

A. Transformer Turn Ratio

Because the proposed converter operating in the PSR mode completely utilizes the switching cycle with the highest efficiency [19], the turn-ratio $N_p : N_s = n$ of T should be selected such that it outputs the desired output voltage V_o at $V_{\mathrm{in}} = V_{\mathrm{nom}}$, as follows:

$$n = \frac{V_o}{2V_{\mathrm{nom}}}. \tag{57}$$

B. Resonant Capacitance and Inductance

For proper converter operation, Δv_{Cr} in (48) must be lower than half of V_o under all operating conditions. And, C_r can be

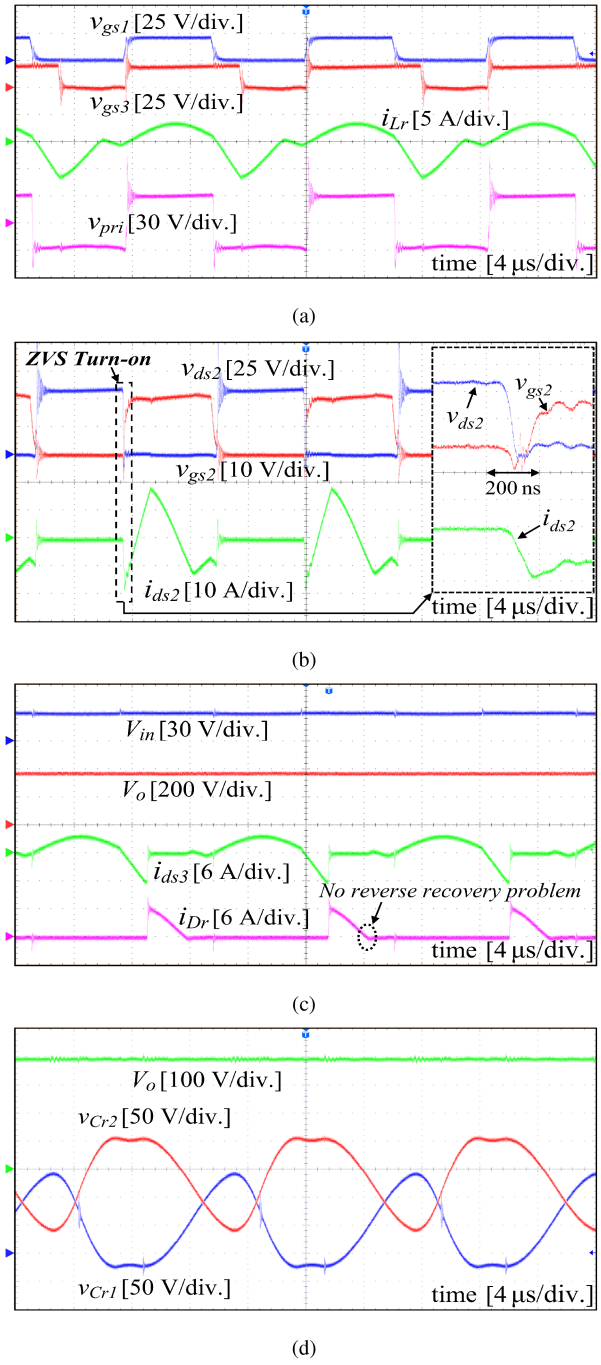

Fig. 8. Waveforms of the proposed resonant converter in the ARB mode.

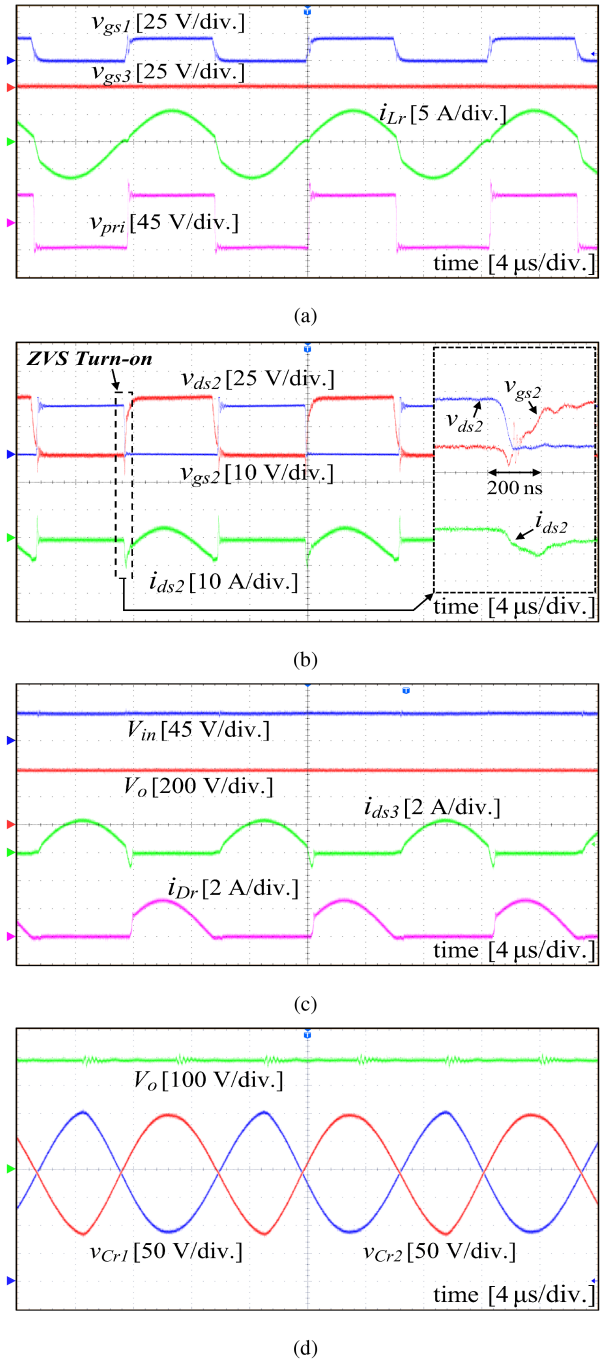

Fig. 9. Waveforms of the proposed resonant converter in the PSR mode.

chosen as

$$C_r \geq \frac{P_o T_s}{V_o^2}. \tag{58}$$

To decrease conduction losses and obtain ZCS of the secondary switches, ω_r must be lower than $\omega_s = 2\pi f_s$. And, by choosing an appropriate ω_r, we can choose L_r from (7) and (58), as follows:

$$L_r \leq \frac{V_o^2}{w_r^2 P_o T_s}. \tag{59}$$

If condition (59) is met, the chosen L_r has to be sufficiently large to ensure the peak of i_{Lr}, which is as small as possible during the ARB mode. If the peak of i_{Lr} is large, S_3 incurs large turn-OFF losses, and thus, the power efficiency gets decreased.

C. Magnetizing Inductance

The magnetizing inductance L_m can be determined based on the input and output power, that is, P_{in} and P_o. If we assume

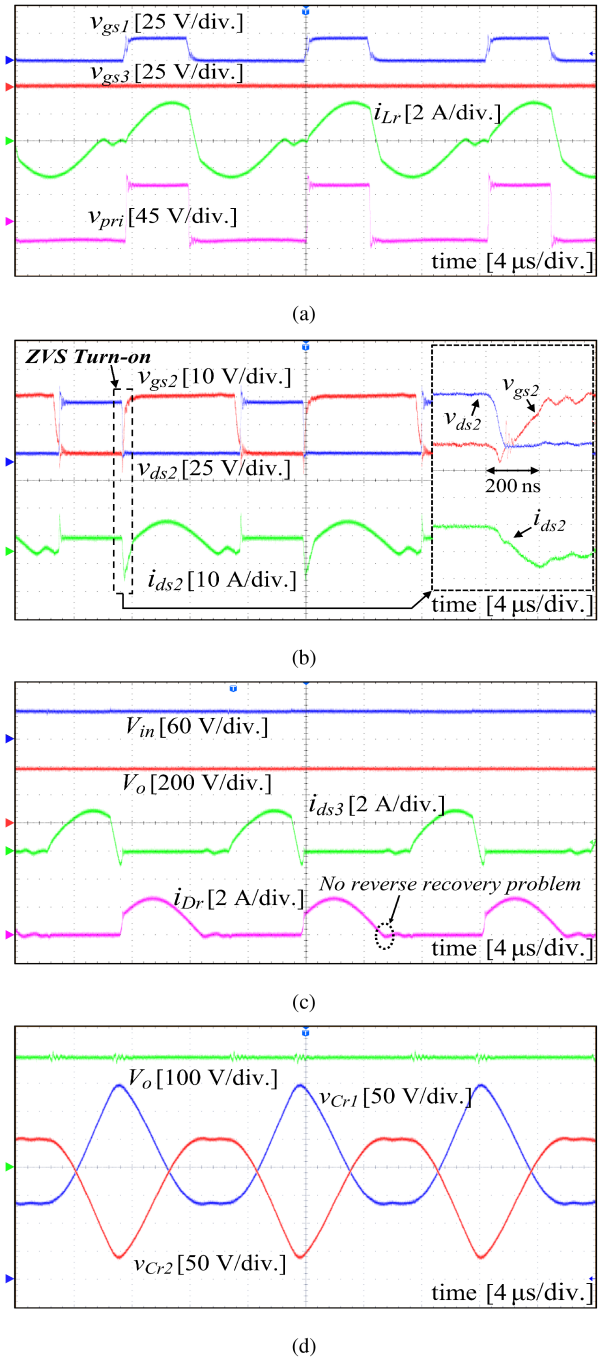

Fig. 10. Waveforms of the proposed resonant converter in the APSRB mode.

that the converter circuit is lossless

$$V_{\text{in}} I_{\text{in}} = \frac{V_o^2}{R_o}. \tag{60}$$

To facilitate the ZVS turn-ON of S_2, i_{Lm} should flow through S_2 during the deadtime; an average value of i_{Lm} should be large to realize continuous conduction mode (CCM) operation for the waveform of i_{Lm}. Note that the triple-mode resonant converter has the minimum value of V_{in} in the ARB mode. Then, I_{Lm} can

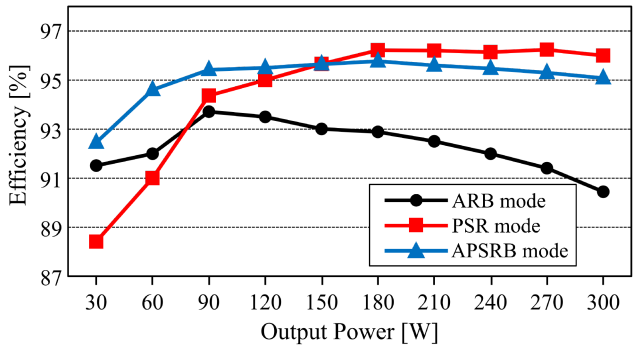

Fig. 11. Efficiency curves of the proposed converter.

TABLE I
PARAMETERS AND COMPONENTS OF THE PROTOTYPE

Parameters	Symbols	Value
Input voltage range	V_{in}	30–60 V
Output voltage	V_o	380 V
Output power	P_o	300 W
Switching frequency	f_s	80 kHz
Resonant frequency	f_r	73.62 kHz
Transformer turns ratio	N_p:N_s	10:47
Magnetizing inductance	L_m	1.56 mH
Resonant inductance	L_r	95.7 μH
Resonant capacitance	C_{r1}, C_{r2}	24.6 nF
Input capacitance	C_{in}	1000 μF
Clamp capacitance	C_C	6.6 μF
Output capacitance	C_o	360 μF
Components	**Symbols**	**Part number**
Primary-side switches	S_1, S_2	IPP050N10N
Secondary-side switch	S_3	UJ3C06505K3S
Secondary-side diode	D_r	CVFD20065A
Transformer core	T	PQ4040

be expressed by solving (60) and $I_{Lm} = I_{\text{in}}/n$, as follows:

$$I_{Lm} = \frac{V_o^2}{nV_{\text{in}}R_o} = \frac{4nV_{\text{in}}M_{\text{ARB}}^2}{R_o}. \tag{61}$$

During $0 < t < D_{\text{pri}}T_s$, the slope of i_{Lm} is nV_{in}/L_m. Then, the ripple of i_{Lm} can be defined as

$$\Delta i_{Lm} = \frac{nV_{\text{in}}D_{\text{pri}}T_s}{2L_m}. \tag{62}$$

To realize the CCM operation, I_{Lm} should always be larger than Δi_{Lm}. Thus, based on (61) and (62), L_m can be selected as

$$L_m > \frac{R_o D_{\text{pri}} T_s}{8M_{\text{ARB}}^2}. \tag{63}$$

V. EXPERIMENTAL RESULTS AND DISCUSSIONS

To validate the performance of the triple-mode resonant converter, we performed experimental tests using a 300-W prototype of the proposed converter with parameters presented in Table I. A digital control algorithm was implemented using a TMS320F28377D control board. The experiments were conducted to validate the triple-mode operation and soft-switching performance under three different operating modes by comparing V_{in} with V_{nom} under full-load conditions.

TABLE II
COMPARISON OF CONVENTIONAL CONVERTERS AND PROPOSED CONVERTER

Items		[12]	[16]	[18]	[19]	[21]	Proposed converter
Topology		Active clamp + Diode bridge rectifier	Full bridge + Voltage doubler with asymmetric structure	Full bridge + Voltage doubler with bidirectional GaN ac switch	Full bridge + Voltage doubler	Active clamp + Bridgeless boost converter	Active clamp + Voltage doubler with asymmetric structure
Number of switches and diodes		2 and 2	5 and 1	5 and 2	6 and 0	4 and 2	3 and 1
Number of passive components		3	4	3	3	2	3
Rated power		400 W	300 W	300 W	600 W	400 W	300 W
Input voltage		375 V	25–35 V	15–55 V	30–55 V	35–65 V	30–60 V
Voltage conversion ratio	Buck	N/A	N/A	$\frac{R_1+\sqrt{R_1^2+8AB}}{4B}$	$\frac{R_1+\sqrt{R_1^2+8AB}}{4B}$	$\frac{R_2+\sqrt{R_2^2+32AB}}{16B(1-D)}$	$\frac{R_3+\sqrt{R_3^2+16AB}}{8B(1-D)}$
	Pure series	$\frac{1}{2(1-D)}$	$\frac{1}{2(1-D)}$	$\frac{1}{2(1-D)}$	$\frac{1}{2(1-D)}$	$\frac{1}{4(1-D)}$	$\frac{1}{2(1-D)}$
	Boost		$\frac{B+\sqrt{B^2+2AB(2-A)}}{B(2-A)}$	$\frac{1+\sqrt{1+\frac{D^2T_sV_o^2}{2L_r}}}{2}$	$\frac{A+B+\sqrt{(1-4B)A^2+6AB+B^2}}{2B(1-A)}$	$\frac{A+B}{2B-AB}$	$\frac{2A+2B}{2B-AB}$
Cost		Low	Medium	High	Medium	Medium	Medium
Modulation complexity		High	Medium	High	High	Medium	Medium
Efficiency		96.1%	99%	98.3%	97.5%	97.6%	96.2%

*Voltage conversion ratio was calculated by $M = V_o/(2nV_{\rm in})$; $R_1 = A(B-1)$, $R_2 = A(B-4)$ and $R_3 = A'(B-2)$.

When $V_{\rm in} = 30$ V, the proposed converter operates in the ARB mode (see Fig. 8). Fig. 8(a) depicts the primary-side voltage $v_{\rm pri}$ of T, resonant current i_{Lr}, gate–source voltage $v_{\rm gs1}$ of S_1, and gate–source voltage v_{gs3} of S_3. During the first half of the switching period, i_{Lr} follows a resonant waveform. After S_1 is turned OFF and S_3 is still turned ON, L_r is charged, and i_{Lr} increases almost linearly. When S_3 is turned OFF, inductor L_r is discharged, and i_{Lr} decreases following a sinusoidal waveform, which eliminates the loss resulting from one turn-OFF loss. Fig. 8(b) illustrates the drain–source voltage $v_{\rm ds2}$ of S_2, gate–source voltage $v_{\rm gs2}$ of S_2, and switch current $i_{\rm ds2}$ of S_2. $i_{\rm ds2}$ is equal to the sum of i_{Lr} and i_{Lm} multiplied by the turns ratio of the transformer during a turn-ON time of S_2. When S_1 is turned OFF, $i_{\rm ds2}$ becomes negative, resulting in ZVS of switch S_2. Fig. 8(c) presents $V_{\rm in}$, V_o, switch current $i_{\rm ds3}$ of S_3, and diode current i_{Dr} of D_r. The converter achieves a zero reverse-recovery current owing to the ZCS of D_r.

When $V_{\rm in} = 45$ V, the proposed converter operates in the PSR mode (see Fig. 9). As S_3 is not used in this mode, i_{Lr} follows an almost sinusoidal waveform without a boost period (i.e., $D_{\rm ARB}T_s = 0$). However, for a light load, i_{Lm} accounts for a large portion of i_{Lr}. S_2 achieves ZVS turn-ON, and the rectifier diode D_r does not suffer from reverse-recovery problems, such as those in the ARB mode.

When $V_{\rm in} = 60$ V, the proposed converter operates in the APSRB mode (see Fig. 10). As S_1 is turned ON and S_2 is turned OFF, i_{Lr} increases. When S_1 is turned OFF and S_2 is turned ON, resonance is terminated, and i_{Lr} rapidly approaches zero. Furthermore, i_{Lr} follows a sinusoidal waveform in the negative direction for the remainder of the switching period. S_2 achieves ZVS turn-ON, and the rectifier diode D_r does not suffer from reverse recovery problems similar to other modes.

Fig. 11 illustrates the power conversion efficiency of the proposed converter in different operating modes depending on the output load. A Yokogawa WT332E digital power meter was used to measure the power conversion efficiency. The proposed converter achieved a maximum efficiency of 96.2% at $P_o = 180$ W in the PSR mode. In the ARB mode, the boosting duty ratio $D_{\rm ARB}$ in (44) changes according to the load condition. Then, the current flowing S_3 continues to increase during the duration $D_{\rm ARB}T_s$ for boosting operation, thereby its high conduction loss in S_3 could result in the power efficiency decrease in the ARB mode. The California Energy Commission weighted efficiency values were 93.7%, 96.2%, and 95.8% under the ARB, PSR, and APSRB modes, respectively.

Table II compares the electrical characteristics and circuit configurations of the proposed triple-mode resonant converter and other resonant converters. The converters presented in [12] and [16] exhibit a relatively narrow input voltage range because they adopt a single-mode operation. As series-resonant converters with triple-mode operation have a wider input voltage range regulation, they are suitable for application in renewable harvesting. Compared with other triple-mode operation converters [18], [19], [21], the proposed converter demonstrates a wider input voltage regulation range while maintaining a small number of components. This feature can reduce the size and cost of the converters, thereby providing a competitive edge for power systems of renewable energy sources.

VI. CONCLUSION

This article presents a triple-mode resonant dc–dc converter using an extended asymmetric modulation operating over a wide input voltage range for application in renewable energy harvesting. This converter has triple-mode operation by comparing the input voltage with a nominal voltage; thereby, it can operate over a wide input voltage range. Furthermore, the proposed converter employs a flyback topology with an active clamp

circuit at the low-voltage side and an asymmetric half-bridge type voltage-doubler at the high-voltage side; it comprises only three switches and one diode with a low transformer turns ratio. Thus, the converter can achieve high power density. Moreover, with the aid of the extended asymmetric modulation, the circuit can halve hard-switching turn-ON losses of the rectifier while keeping the small number of switch components. A 300-W prototype was built and tested to confirm the validity of the proposed converter. Within the specified operating range, the converter achieved above 95% peak efficiency under both the PSR and APSRB modes. As a result, the proposed converter is suitable for renewable energy applications such as thermoelectric and photovoltaic energy, which generate a relatively low and fluctuating dc voltage. In addition, because the proposed converter features high power density, it can achieve much higher power capacity through modularization.

REFERENCES

[1] F. H. Gandomana et al., "Review of FACTS technologies and applications for power quality in smart grids with renewable energy systems," *Renewable Sustain. Energy Rev.*, vol. 82, no. 1, pp. 502–514, Feb. 2018.

[2] K. Tian, S. Ali, Z. Huang, and Z. Ling, "Power control and experiment of 2MW/10 kV cascaded H-bridge power conversion system for battery energy storage system," in *Proc. 8th Renewable Power Gener. Conf.*, 2019, pp. 1–7.

[3] M. Kim, H. Jeong, B. Han, and S. Choi, "New parallel loaded resonant converter with wide output voltage range," *IEEE Trans. Power Electron.*, vol. 33, no. 4, pp. 3106–3114, Apr. 2018.

[4] Y. Shen, H. Wang, A. Al-Durra, Z. Qin, and F. Blaabjerg, "A structure-reconfigurable series resonant DC–DC converter with wide-input and configurable-output voltages," *IEEE Trans. Ind. Appl.*, vol. 55, no. 2, pp. 1752–1764, Mar./Apr. 2019.

[5] Z. Saadatizadeh, P. C. Heris, M. Sabahi, and E. Babaei, "A DC–DC transformerless high voltage gain converter with low voltage stresses on switches and diodes," *IEEE Trans. Power Electron.*, vol. 34, no. 11, pp. 10600–10609, Nov. 2019.

[6] Z. Zhang and K. D. Ngo, "Multi-megahertz quasi-square-wave flyback converter using eGaN FETs," *IET Power Electron.*, vol. 10, no. 10, pp. 1138–1146, Jun. 2017.

[7] Z. Zhang, S. Tian, and K. D. T. Ngo, "Small-signal equivalent circuit model of quasi-square-wave flyback converter," *IEEE Trans. Power Electron.*, vol. 32, no. 8, pp. 5885–5888, Aug. 2017.

[8] R. Watson, F. C. Lee, and G. C. Hua, "Utilization of an active-clamp circuit to achieve soft switching in flyback converters," *IEEE Trans. Power Electron.*, vol. 11, no. 1, pp. 162–169, Jan. 1996.

[9] J. Zhang, X. Huang, X. Wu, and Z. Qian, "A high efficiency flyback converter with new active clamp technique," *IEEE Trans. Power Electron.*, vol. 25, no. 7, pp. 1775–1785, Jul. 2010.

[10] Y.-K. Lo and J.-Y. Lin, "Active-clamping ZVS flyback converter employing two transformers," *IEEE Trans. Power Electron.*, vol. 22, no. 6, pp. 2416–2423, Nov. 2007.

[11] H. Tarzamni, E. Babaei, and A. Z. Gharehkoushan, "A full soft-switching ZVZCS flyback converter using an active auxiliary cell," *IEEE Trans. Ind. Electron.*, vol. 64, no. 2, pp. 1123–1129, Feb. 2017.

[12] J.-J. Lee, J.-M. Kwon, E.-H. Kim, and B.-H. Kwon, "Dual series-resonant active clamp converter," *IEEE Trans. Ind. Electron.*, vol. 55, no. 2, pp. 699–710, Feb. 2008.

[13] S. Son, O. A. Montes, A. Junyent-Ferre, and M. Kim, "High step-up resonant DC/DC converter with balanced capacitor voltage for distributed generation systems," *IEEE Trans. Power Electron.*, vol. 34, no. 5, pp. 4375–4387, May 2019.

[14] J. Hassan, C. Bai, J. W. Lim, and M. Kim, "High step-up quasi-resonant converter featuring minimized switching loss over wide input voltage range," *IEEE Trans. Ind. Electron.*, vol. 68, no. 11, pp. 10784–10795, Nov. 2021.

[15] C. Bai, B. Han, B. Kwon, and M. Kim, "Highly efficient bidirectional series-resonant DC/DC converter over wide range of battery voltages," *IEEE Trans. Power Electron.*, vol. 35, no. 4, pp. 3636–3650, Apr. 2020.

[16] J. Kim, M. Park, J. Han, M. Lee, and J. Lai, "PWM resonant converter with asymmetric modulation for ZVS active voltage doubler rectifier and forced half resonance in PV application," *IEEE Trans. Power Electron.*, vol. 35, no. 1, pp. 508–521, Jan. 2020.

[17] T. LaBella, W. Yu, J. S. Lai, M. Senesky, and D. Anderson, "A bidirectional-switch-based wide-input range high-efficiency isolated resonant converter for photovoltaic applications," *IEEE Trans. Power Electron.*, vol. 29, no. 7, pp. 3473–3484, Jul. 2014.

[18] T. LaBella and J. S. Lai, "A hybrid resonant converter utilizing a bidirectional GaN AC switch for high-efficiency PV applications," *IEEE Trans. Ind. Appl.*, vol. 50, no. 5, pp. 3468–3475, Sep./Oct. 2014.

[19] S. Kim, B. Kim, B. H. Kwon, and M. Kim, "An active voltage-doubler rectifier based hybrid resonant DC/DC converter for wide-input-range thermoelectric power generation," *IEEE Trans. Power Electron.*, vol. 33, no. 11, pp. 9470–9481, Nov. 2018.

[20] X. Zhao, L. Zhang, R. Born, and J. Lai, "A high-efficiency hybrid resonant converter with wide-input regulation for photovoltaic applications," *IEEE Trans. Ind. Electron.*, vol. 64, no. 5, pp. 3684–3695, May 2017.

[21] J. Kim, S. W. Ryu, M. Kim, and J. W. Jung, "Triple-mode isolated resonant buck–boost converter over wide input voltage range for residential applications," *IEEE Trans. Ind. Electron.*, vol. 68, no. 11, pp. 11087–11099, Nov. 2021.

Sangoh Kim (Student Member, IEEE) was born in Daegu, South Korea, in 1996. He received the B.S. degree in electronics engineering in 2020 and the M.S. degree in electronic and electrical engineering in 2022 from Kyungpook National University, Daegu, where he is currently working toward the Ph.D. degree in electronic and electrical engineering.

His research interests include high-efficiency power conversion and control, power circuit design, and renewable energy systems.

Junseong Cho (Student Member, IEEE) was born in Changwon, South Korea, in 1996. He received the B.S. degree in electronic engineering from Daegu University, Gyeongsan, South Korea, in 2021, and the M.S. degree in electronics and electrical engineering from Kyungpook National University, Daegu, South Korea, in 2023.

He is currently an Associate with System Development Center, Hanwha Solution, Daegu. His research interests include battery charger systems, renewable energy systems, and grid-connected inverters.

Jong-Woo Kim (Member, IEEE) received the B.S., M.S., and Ph.D. degrees in electrical engineering from the Korea Advanced Institute of Science and Technology (KAIST), Daejeon, South Korea, in 2010, 2012, and 2016, respectively.

From 2016 to 2019, he was a Research Assistant Professor and a Postdoctoral Researcher with Virginia Tech, Blacksburg, VA, USA. From 2019 to 2021, he was a Member of R & D Staf, Milan M. Jovanović Power Electronics Laboratory, Delta Electronics (Americas), Research Triangle Park, NC, USA. From 2021 to 2022, he was a Power Hardware Engineer with Meta (formerly Facebook), Menlo Park, CA, USA. Since 2022, he has been an Assistant Professor with Konkuk University, Seoul, South Korea. He has authored or coauthored 22 journal articles and more than 20 technical papers in conference proceedings. His research interests include high-efficiency power converters, high-power-density design with magnetic component integration/PCB winding/wide-bandgap devices, EMI noise reduction techniques, and analog/digital control for data center power and electric vehicle charging infrastructure.

Minsung Kim (Senior Member, IEEE) was born in Ulsan, South Korea, in 1986. He received the B.S. and Ph.D. degrees in electrical engineering from the Pohang University of Science and Technology (POSTECH), Pohang, South Korea, in 2008 and 2013, respectively.

Since 2013, he has been with the Department of Creative IT Engineering and Future IT Research Laboratory, POSTECH, where he was a Research Assistant Professor. In 2016, he was a Research Scholar with Future Energy Electronics Center, Virginia Tech, Blacksburg, VA. In 2017 and 2018, he was also an Academic Visitor with Control and Power System Group, Imperial College London, London, U.K. Since 2018, he has been with the Division of Electronics and Electrical Engineering, Dongguk University, Seoul, South Korea, where he is currently an Assistant Professor. His current research interests include highly efficient power conversion circuit design, intelligent controller design for industrial electronics, and renewable energy and energy storage systems.

Byeongcheol Han (Member, IEEE) was born in Busan, South Korea, in 1986. He received the B.S. degree in electrical engineering from Pusan National University, Busan, in 2012, and the Ph.D. degree in creative IT engineering (CiTE) from the Pohang University of Science and Technology (POSTECH), Pohang, South Korea, in 2018.

In 2018, he was a Postdoctoral Researcher in CiTE with POSTECH. From 2018 to 2020, he was a Postdoctoral Associate with Future Energy Electronics Center (FEEC), Virginia Tech, Blacksburg, VA, USA. He is currently an Assistant Professor with the School of Electronics Engineering, Kyungpook National University, Daegu, South Korea. His research interests include GaN-based power electronic circuit design, modulation techniques for EMI noise reduction, nonlinear systems and control, grid-connected inverters, and advanced control design for power-conversion systems.